PAPER

Check for updates

Comparative study of the therapeutic potential of C$_{24}$, C$_{32}$, B$_{12}$N$_{12}$, and B$_{16}$N$_{16}$ nanocages as drug delivery carriers for delivering an erlotinib derivative: DFT and QTAIM investigations†

Khourshid Mehdizadeh, [ID] [a] Sourour PourFalatoon,[b] Milad Nouraliei,[c] Majid Farsadrooh, [ID] *[d] Hanseung Kim,[e] Marzieh Ramezani Farani [ID] *[e] and Yun Suk Huh [ID] *[e]

The use of nanostructures as drug delivery vehicles for a wide range of anticancer medications to lessen their severe side effects by delivering them to the targeted tumor cell location is presently a broadly studied innovative biomedical application of different nanostructures. To investigate the capability of C$_{24}$ and C$_{32}$, B$_{12}$N$_{12}$, and B$_{16}$N$_{16}$ nanocages as nanocarriers for delivering the methyl erlotinib molecule, we conducted density functional theory (DFT) computations using the M06-2X/6-311G(d,p) and M06-2X/6-31G(d) levels of theory. The calculation of the adsorption energy of methyl erlotinib on the nanocages was performed in aqueous and gaseous phases. The adsorption energy values associated with the interaction between the nanocages and methyl erlotinib were negative, indicating that this interaction was exothermic in nature. The adsorption energy values in the aqueous state were higher than those in the gaseous state, suggesting a stronger interaction in the aqueous state, with the exception of the C$_{32}$ nanocage. Analyses of the density of states (DOS) and projected density of states (PDOS) were performed in order to examine the effect of methyl erlotinib adsorption on the electronic characteristics of selected nanocages. The findings indicated that the B$_{12}$N$_{12}$ nanocage following methyl erlotinib molecule adsorption came nearer to the Fermi level than the other nanocages examined. Calculations based on the Quantum Theory of Atoms in Molecules (QTAIM) indicated that methyl erlotinib had a weak interaction with all selected nanocages. According to the values of the adsorption energy derived from both methodologies, the interaction between methyl erlotinib and the B$_{12}$N$_{12}$ nanocage was determined to be more robust than the interaction between methyl erlotinib and the C$_{24}$ nanocage, while the interaction between methyl erlotinib and the B$_{16}$N$_{16}$ nanocage was also stronger than that with the C$_{32}$ nanocage. Notable variations in the ΔE_g values were detected for methyl erlotinib@B$_{12}$N$_{12}$ and methyl erlotinib@B$_{16}$N$_{16}$ across all methods, suggesting that the conductivity of these two nanostructures improved more significantly following the adsorption of methyl erlotinib than that of other nanostructures. Consequently, the B$_{12}$N$_{12}$ and B$_{16}$N$_{16}$ nanocages can function as nanosensors for methyl erlotinib.

[a]*Department of Chemistry, Roudsar and Amlash Branch, Islamic Azad University, Roudsar, Iran*

[b]*Department of Chemistry, Science and Research Branch, Islamic Azad University, Tehran, Iran*

[c]*Department of Chemistry, Islamic Azad University, Central Tehran Branch, Tehran, Iran*

[d]*Renewable Energies Research Laboratory, Department of Chemistry, Faculty of Science, University of Sistan and Baluchestan, P.O. Box 98135 674, Zahedan, Iran. E-mail: farsadroohmajid@gmail.com; Tel: +989111369044*

[e]*NanoBio High-Tech Materials Research Center, Department of Biological Sciences and Bioengineering, Inha University, Incheon 22212, Republic of Korea. E-mail: farani.marzi@inha.ac.kr, yunsuk.huh@inha.ac.kr; Tel: +82-10-9609-1367, +82-10-9633-6377*

†Electronic supplementary information (ESI) available. See DOI: https://doi.org/10.1039/d4nr05393a

1. Introduction

Cancer is a crucial global health issue marked by the uncontrolled proliferation and spread of abnormal cells, and it remains a primary cause of death worldwide.[1] Lung cancer is the most common type of cancer globally and the leading cause of cancer-related deaths. Lung cancer can be categorized into two main types based on its histopathological characteristics: non-small cell lung cancer (NSCLC) and small cell lung cancer (SCLC), with NSCLC accounting for approximately 80% of all clinical lung cancer cases.[2] A significant proportion of NSCLC patients harbor mutations in the epidermal growth factor receptor (EGFR), with estimates indicating that around 40%–60% of these individuals are of Asian origin.[3] EGFR tyro-

sine kinase inhibitors, including gefitinib, afatinib, and erlotinib, have shown significant efficacy in treating NSCLC patients with EGFR-activating mutations, which have led to remarkable treatment responses. Erlotinib, a quinazoline derivative chemically known as N-(3-ethynylphenyl)-6,7-bis(2-methoxyethoxy)-4-quinazolinamine, reversibly and selectively inhibits the EGFR tyrosine kinase, thereby blocking downstream signaling pathways involved in angiogenesis, metastasis, and cell proliferation.[4–6] Approved by the U.S. FDA in 2004 for the treatment of pancreatic cancer and metastatic NSCLC,[5] erlotinib binds reversibly to the adenosine triphosphate (ATP) binding site within the tyrosine kinase domain of the EGFR, inhibiting auto-phosphorylation and promoting apoptosis, suppressing angiogenesis, and preventing excessive cell proliferation.[7,8] However, poor water solubility of erlotinib and extensive metabolism, primarily by CYP3A4 enzymes in the intestines and liver, result in reduced and inconsistent bioavailability (59%).[9] This necessitates higher doses to achieve effective tumor growth inhibition, which in turn is associated with common side effects such as anemia, Stevens–Johnson syndrome, neutropenia, mucositis, headaches, diarrhea, and skin rash.[9–11] Therefore, developing a delivery system that enhances efficacy at reduced doses is crucial for mitigating side effects and preventing or delaying acquired resistance.

Nanoscale drug delivery systems have emerged as a promising approach for addressing the challenges associated with chemotherapy. These systems offer several advantages, including reduced toxicity, lower effective doses, and specific targeting of tumor sites. These systems can bypass physiological barriers, evade drug resistance mechanisms, and release drugs precisely at the tumor site, often triggered by specific stimuli. The enhanced permeability and retention (EPR) effect, first identified in 1986, allows drug-loaded carriers to accumulate at tumor sites due to the significantly higher vascular permeability in tumors compared to normal tissues. Nanoscale drug delivery systems offer several advantages, including reduced toxicity to healthy cells, lower effective doses, and the ability to specifically target tumor sites.

Among the various nanostructures explored for drug delivery, fullerenes, carbon nanotubes,[12,13] and boron nitride fullerenes have garnered significant attention due to their unique properties. Fullerenes, a distinctive group of carbon allotropes, exhibit attractive photochemical, electrochemical, and physical characteristics, making them promising candidates for nanoscale drug carriers.[14,15] Their significant apolar nature facilitates drug absorption, while their low toxicity and biocompatibility enhance metabolic efficacy and make them suitable for medical applications.[16] Additionally, non-covalent interactions, such as π–π stacking, between fullerenes and the aromatic rings of drug molecules further enhance their drug delivery potential.[17] The small size of fullerenes provides significant benefits, including modified pharmacokinetic properties and enhanced payload capacity, compared to conventional drug delivery systems.[18] In summary, fullerenes are utilized in drug delivery due to their ability to (i) enable effective drug incorporation and release, (ii) enhance formulation stability and shelf life, (iii) exhibit biocom-

patibility, (iv) facilitate biodistribution and targeting, and (v) offer functional versatility.[19] Similarly, boron nitride (BN) fullerenes, which share isoelectronic similarities with carbon fullerenes, have gained attention for their chemical stability and unique properties. The ionic bonds between positively charged boron atoms and negatively charged nitrogen atoms contribute to their stability,[20] while the sp^3 hybridization of nitrogen atoms with boron atoms results in locally pyramidal geometries.[21] These structural features enable BN fullerenes to interact with other molecules through physical or chemical binding, making them suitable for drug delivery applications. Recent theoretical studies have demonstrated the responsiveness of BN nanocages to biomolecules, highlighting their potential as biochemical sensors.[22]

The primary aim of this research is to examine the adsorption behavior of methyl erlotinib molecules onto the C_{24}, C_{32}, $B_{12}N_{12}$, and $B_{16}N_{16}$ nanocages as potential drug delivery carriers, as well as the anticancer properties of their complexes, using density functional theory (DFT) and molecular docking simulations. The quantum theory of atoms in molecules (QTAIM) was employed to analyze the interactions between methyl erlotinib and the nanocages. Additionally, to understand the impact of nanocage volume on drug adsorption, C_{24} and C_{32} nanocages were selected for comparative analysis.

2. Computational methods

C_{24}, $B_{12}N_{12}$, C_{32}, and $B_{16}N_{16}$ fullerenes were selected as nanocarriers to investigate their ability to deliver the methyl erlotinib drug. GAMESS-US software was used to perform DFT calculations utilizing the M06-2X approach with the basis sets of 6-311G(d,p) and 6-31G(d).[23–25] The objective was to conduct natural bond orbital (NBO) analysis,[26] as well as to obtain the outcomes of the density of states (DOS) and the levels of molecular electrostatic potential.[27,28] Furthermore, we sought to identify the characteristics of the interaction between the medication and the nanostructures by employing calculations derived from the QTAIM. DFT calculations were conducted based on the ground state of the compounds. Additionally, the compounds were assigned a charge of 0 and a spin of 1 (singlet). Software tools Gauss View 5.0 and Nanotube Modeler were employed to simulate nanotubes and interact with their structures. Using GaussSum v3.0 software,[29] we plotted density of states (DOS) diagrams. The following equation was employed to determine the energy of adsorption (E_{ads}) of methyl erlotinib molecules at the selected nanocages:[21,30]

$$E_{ads} = (E_{complex}) - (E_{nanostructure} + E_{drug}) \quad (1)$$

where $E_{nanostructure}$ and $E_{complex}$ refer to the primary energy value of nanostructures and the total energy of methyl erlotinib combined with nanostructures, respectively. E_{drug} represents the primary energy value of methyl erlotinib. A negative adsorption energy value signifies that the process is exothermic in nature. The characteristics of bond critical points (BCP) were determined using QTAIM calculations. The AIM2000 program was applied to analyze the optimized complexes and

the kinds of atoms and molecules participating in the interaction. QTAIM calculations can accurately identify chemical properties and various types of interactions and bonds.[31,32] This approach was employed to analyze interactions between atoms, evaluate charge density ($\rho(r)$), assess the Laplacian of the charge density ($\nabla^2\rho(r)$), examine intermolecular interactions, and identify bond critical points. To modify for the basis set superposition error (BSSE) in the adsorption energy, we employed the counterpoise approach. Molecular docking (MD) simulations were conducted to investigate the interactions between erlotinib derivatives and the tyrosine kinase enzyme (TKI). The 3D structures of TKI targets were acquired from the Protein Data Bank (PDB) utilizing the code 8E4T. Five ligands derived from erlotinib were obtained from the PubChem database, as shown in Table 2. The AutoDock4 package was utilized to conduct molecular dynamics (MD) simulations using a genetic algorithm with 100 conformational searches within a grid box that measures $40 \times 40 \times 40$.[33,34]

3. Results and discussion

3.1. Adsorption of methyl erlotinib onto the C_{24} nanocage

The optimum C_{24} nanocage geometric shape is composed of eight hexagonal rings and six quadrilateral rings. In the tetragonal rings, the C–C bonds were 1.48 Å long, whereas in the hexagonal rings, the C–C and C=C bonds were 1.48 Å and 1.37 Å long, respectively. The C_{24} nanocage studied consisted of 24 carbon atoms. The methyl erlotinib molecule was initially positioned in multiple locations on the outer surface of the C_{24} nanocage, each with distinct orientations. Fig. 2a depicts the most stable and best position of methyl erlotinib on the C_{24} nanocage surface. Analysis based on natural bond orbital (NBO) techniques suggested that positive charge transfer (Q_T) occurs in the C_{24} fullerene. The findings indicate that charge is transferred from methyl erlotinib to the C_{24} nanocage. Following the adsorption process, the energy gap (E_g) of the C_{24} nanocage was diminished. This reduction in the energy gap (E_g) suggests that the conductivity of the C_{24} nanocage has improved.

Fig. 1 displays the optimum structures for the methyl erlotinib molecule and the C_{24}, C_{32}, $B_{12}N_{12}$, and $B_{16}N_{16}$ nanocages. The methyl erlotinib molecule was initially positioned at multiple locations on the outer surface of the C_{24} nanocage, exploring different orientations. The most stable and optimal orientation of methyl erlotinib on the surface of C_{24} is depicted in Fig. 2a. Table 1 presents the calculated values for adsorption energy (E_{ads}), energy gap (E_g), and the variation in the energy gap of the nanostructures before and after the adsorption of methyl erlotinib (ΔE_g). The analysis conducted using NBO reveals a positive transferred charge (Q_T), indicating that charge transfer occurs from methyl erlotinib to the C_{24} atom. The energy gap value (E_g) in C_{24} diminished following adsorption, suggesting alterations in its conductivity compared to the state prior to adsorption. The calculated values of E_{ads} for both the gaseous and aqueous states reveal that methyl erlotinib was chemically adsorbed onto the surface of C_{24}. The negative
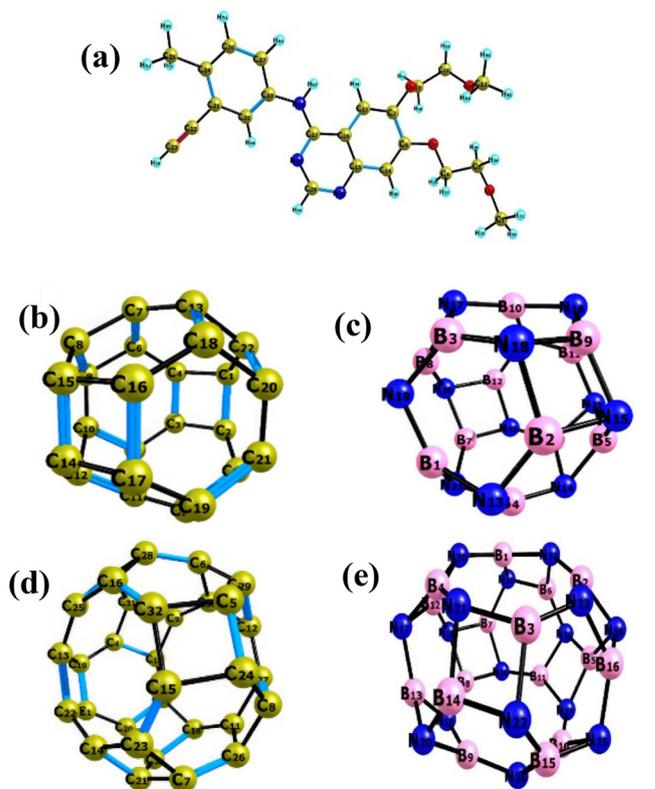

Fig. 1 Optimized structures of (a) the methyl erlotinib molecule, (b) C_{24} nanocage, (c) $B_{12}N_{12}$ nanocage, (d) C_{32} nanocage and (e) $B_{16}N_{16}$ nanocage.

adsorption energy values of methyl erlotinib in both aqueous and gaseous states signify that its adsorption on the C_{24} nanocage is exothermic. The obtained adsorption energy for methyl erlotinib on C_{24} indicates that C_{24} could serve as a suitable nanocarrier for delivering the methyl erlotinib molecule.

3.2. Methyl erlotinib adsorption onto the $B_{12}N_{12}$ nanocage

The $B_{12}N_{12}$ nanocage being examined consisted of 12 nitrogen atoms and 12 boron atoms. The optimal structure of the $B_{12}N_{12}$ nanostructure is composed of eight hexagonal rings and six quadrilateral rings. The B–N bond lengths were found to be 1.480 Å and 1.430 Å in the hexagonal rings and 1.480 Å in the tetragonal rings. The molecule of methyl erlotinib was initially positioned in different locations on the outer surface of the $B_{12}N_{12}$ nanocage utilizing varying orientations. The optimal and most stable placement of methyl erlotinib on the surface of the $B_{12}N_{12}$ nanocage is depicted in Fig. 2b. There was a 2.2490 eV increase in the HOMO energy level following interaction with methyl erlotinib. This suggests that methyl erlotinib likely acts as an electron acceptor, while the $B_{12}N_{12}$ nanocage functions as an electron donor. On the other hand, the nitrogen atoms (atomic numbers 16, 24, 17, and 24) and boron atom (atomic number 10) in the $B_{12}N_{12}$ nanostructure interact with the oxygen atom (atomic number 35) and the hydrogen atoms (atomic numbers 66, 64, 69, and 59) of methyl erlotinib. In the $B_{12}N_{12}$ nanocage, electron transfer is much easier
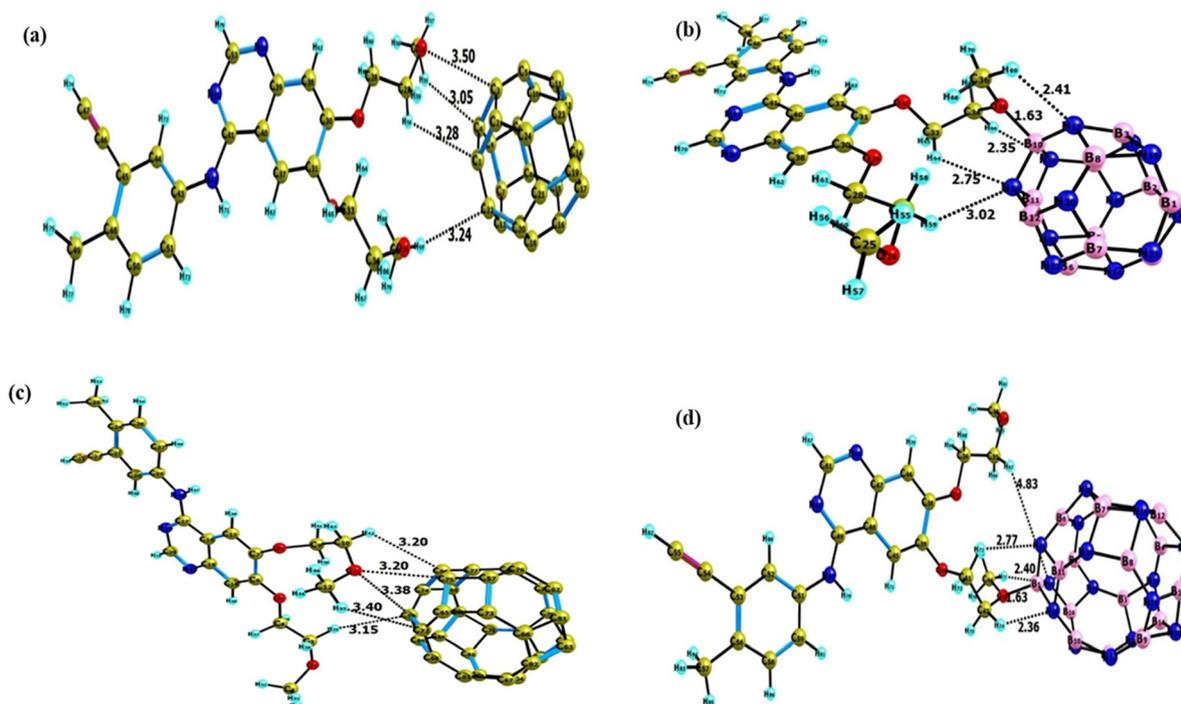
Fig. 2 Optimized structures of (a) the methyl erlotinib@C_{24} nanocage, (b) methyl erlotinib@$B_{12}N_{12}$ nanocage, (c) methyl erlotinib@C_{32} nanocage, and (d) methyl erlotinib@$B_{16}N_{16}$ nanocage.

Table 1 Adsorption energy (E_{ads}) of methyl erlotinib onto the C_{24}, $B_{12}N_{12}$, C_{32}, and $B_{16}N_{16}$ nanocages in aqueous and gaseous phases: BSSE, charge transfer (Q_T), HOMO–LUMO energy gaps (E_g), and changes in the HOMO–LUMO gap energy during adsorption (M06-2X/6-31G(d))

Nanostructures	HOMO (eV)	LUMO (eV)	E_{ads} (eV) in gas	E_{ads} (eV) in water	BSSE (eV)	E_g (eV)	ΔE_g (eV)	Q_T (e)
C_{24} nanocage	−7.133	−2.653	—	—	—	4.480	—	—
$B_{12}N_{12}$ nanocage	−9.278	+0.160	—	—	—	9.439	—	—
C_{32} nanocage	−6.890	−3.259	—	—	—	3.631	—	—
$B_{16}N_{16}$ nanocage	−9.313	−0.209	—	—	—	9.104	—	—
Methyl erlotinib@C_{24} nanocage	−6.823	−2.669	−0.084	−0.1063	0.002	4.153	−0.326	+0.003
Methyl erlotinib@$B_{12}N_{12}$ nanocage	−7.029	−0.819	−1.144	−1.2269	0.008	6.210	−3.229	−0.003
Methyl erlotinib@C_{32} nanocage	−6.801	−3.180	−0.150	−0.136	0.0018	3.620	−0.010	+0.006
Methyl erlotinib@$B_{16}N_{16}$ nanocage	−7.035	−0.827	−1.112	−1.419	0.0034	6.208	−2.896	−0.003

than in the C_{24} nanocage. As a result, the $B_{12}N_{12}$ nanocage has considerably higher adsorption energy than the C_{24} nanocage. The charge transfer (Q_T) obtained from the NBO analysis was found to be negative (Table 1), suggesting that methyl erlotinib acts as an electron acceptor within the methyl erlotinib@$B_{12}N_{12}$ configuration. The energy gap (E_g) showed a notable reduction following the adsorption process. The evaluation of E_{ads} values in both aqueous and gaseous states indicates that methyl erlotinib has a stronger affinity for $B_{12}N_{12}$ compared to C_{24}, $B_{16}N_{16}$, and C_{32}. In both the aqueous and gaseous phases, the adsorption energies of methyl erlotinib were negative, signifying that the binding process of methyl erlotinib to $B_{12}N_{12}$ is exothermic. The values of the adsorption energy of methyl erlotinib on $B_{12}N_{12}$ indicate that its binding occurs through chemisorption, resulting in a significant enhancement of $B_{12}N_{12}$'s conductivity. Thus, $B_{12}N_{12}$ can be used in drug delivery as a recognition system for methyl erlotinib molecules.

3.3. Methyl erlotinib adsorption onto the C_{32} nanocage

There are four different kinds of carbon–atom bonds in the optimal geometric shape of the C_{32} nanocage. In hexagonal structures, the lengths of C–C bonds were found to be 1.48 Å, 1.38 Å, and 1.45 Å, while in octagonal configurations, the C–C bond lengths were found to be 1.52 Å and 1.38 Å. The C_{32} nanocage studied consisted of 32 carbon atoms. The methyl erlotinib molecule was initially positioned in multiple locations on the outer surface of the C_{32} nanocage, employing various orientations. The most stable and optimal binding site of methyl erlotinib on the C_{32} nanocage is illustrated in Fig. 2c. The analysis using NBO indicated that the charge transfer (Q_T) in the C_{32} nanocage was positive. This suggests that there is a transfer of charge from methyl erlotinib to the C_{32} nanocage. The adsorption process led to a reduction in the energy gap value (E_g) of the C_{32} nanocage. The reduction in E_g

3.4. Methyl erlotinib adsorption onto the $B_{16}N_{16}$ nanocage

The $B_{16}N_{16}$ nanocage being examined consisted of 16 nitrogen atoms and 16 boron atoms. In the optimized geometric structure of the $B_{16}N_{16}$ nanocage, five distinct kinds of B–N bonds with varying lengths can be identified. The lengths of B–N bonds in the hexagonal structure were found to be 1.46 Å, 1.43 Å, and 1.50 Å, while in the octagonal configurations, the lengths of B–N bonds were found to be 1.48 Å and 1.43 Å. The methyl erlotinib molecule was initially situated in multiple positions on the outer surface of $B_{16}N_{16}$, with varying orientations. The most stable and optimal binding site of methyl erlotinib on the surface of $B_{16}N_{16}$ is illustrated in Fig. 2d. There was a 2.2781 eV increase in the HOMO energy level following interaction with methyl erlotinib. This suggests that methyl erlotinib likely acts as an electron acceptor, while the $B_{16}N_{16}$ nanocage functions as an electron donor. On the other hand, in the $B_{16}N_{16}$ nanocage, the boron atom (atomic number 5) and the nitrogen atoms (atomic numbers 26, 27, and 31) interact with the oxygen atom (atomic number 43) and the hydrogen atoms (atomic numbers 67, 72, 74, and 77) of methyl erlotinib. In the $B_{16}N_{16}$ nanocage, electron transfer is much easier than in the C_{32} nanocage. As a result, the $B_{16}N_{16}$ nanocage has considerably higher adsorption energy than the C_{32} nanocage. The charge transfer (Q_T) obtained from the NBO analysis was found to be negative (Table 1), suggesting that methyl erlotinib acts as an electron acceptor within the methyl erlotinib@$B_{16}N_{16}$ configuration. The energy gap (E_g) showed a notable reduction following the adsorption process. The evaluation of E_{ads} values in both aqueous and gaseous states indicates that methyl erlotinib has a stronger affinity for $B_{16}N_{16}$ than C_{24} and C_{32}. In both the aqueous and gaseous phases, the adsorption energies of methyl erlotinib were negative, signifying that the binding process of methyl erlotinib to $B_{16}N_{16}$ is exothermic. The values of adsorption energy of methyl erlotinib on $B_{16}N_{16}$ indicate that its binding occurs through chemisorption, resulting in a significant enhancement of $B_{16}N_{16}$'s conductivity. Based on the analysis, the $B_{16}N_{16}$ nanocage could serve as an effective recognition platform for targeting and delivering methyl erlotinib, a drug molecule, to the desired locations.

3.5. Projected density of states (PDOS) and density of states (DOS)

To investigate how the surface adsorption of the methyl erlotinib molecule affects the electronic properties of nanocages, the DOS was analyzed. Moreover, the primary factor characterizing the interaction between the methyl erlotinib molecule and selected nanocages is the projected density of states (PDOS) spectra, which are associated with the atoms involved in the active sites. The results of PDOS are presented in Fig. S1.† The DOS diagrams of the C_{24}, methyl erlotinib@C_{24}, $B_{12}N_{12}$, methyl erlotinib@$B_{12}N_{12}$, C_{32}, methyl erlotinib@C_{32}, $B_{16}N_{16}$ and methyl erlotinib@$B_{16}N_{16}$ nanostructures are depicted in Fig. 3(a–h). Following the interaction between the

nanocages and methyl erlotinib, the findings indicated that the LUMO and HOMO energy levels of the $B_{12}N_{12}$ and $B_{16}N_{16}$ nanocages approached the Fermi energy level (represented by the yellow line) more closely than those of the other nanostructures. Under optimal conditions, the adsorption of methyl erlotinib onto the C_{24}, $B_{12}N_{12}$, C_{32}, and $B_{16}N_{16}$ nanocages resulted in ΔE_g values of −0.3269 eV, −3.2296 eV, −0.0106 eV, and −2.8966 eV, respectively. The DOS diagrams illustrate that the adsorption of the methyl erlotinib molecules onto the $B_{12}N_{12}$ nanostructure results in a modification of the energy gap. According to the DOS analysis presented in Table 1, the valence and conduction levels of molecular orbitals in the methyl erlotinib@$B_{12}N_{12}$ nanocage and the methyl erlotinib@$B_{16}N_{16}$ nanocage were found to be closer to lower and higher energy levels, respectively. As a result, the energy gap values of the $B_{12}N_{12}$ and $B_{16}N_{16}$ nanocages decreased more significantly than those of the C_{24} and C_{32} nanocages. Additionally, compared to other nanostructures, the valence level of the $B_{12}N_{12}$ nanocage in the methyl erlotinib@$B_{12}N_{12}$ nanocage was closer to the Fermi level. As a result of the interaction, the $B_{12}N_{12}$ nanocage's conductivity increased more significantly in comparison with the other nanostructures. The following equation can be used to determine the electrical conductivity (σ) of molecular complexes at a specific temperature:[12]

$$\sigma \propto \exp\left(\frac{-E_g}{2KT}\right) \qquad (2)$$

In this case, electrical conductivity is denoted by σ. Temperature and the Boltzmann constant are denoted by K and T. According to eqn (2), a lower value of E_g at a given hypothetical temperature results in an increased electrical conductivity. The adsorption of methyl erlotinib onto $B_{16}N_{16}$ and $B_{12}N_{12}$ results in a significant reduction in E_g. Since conductivity is directly related to the reduction in the E_g value, it can be inferred that a decrease in the E_g value leads to an increase in conductivity. The electrical properties of the $B_{12}N_{12}$ and $B_{16}N_{16}$ nanocages become quite pronounced following the adsorption of the methyl erlotinib molecule. Consequently, the $B_{12}N_{12}$ and $B_{16}N_{16}$ nanocages serve not only as potential drug delivery systems for methyl erlotinib but may also function as detectors or nanosensors for this compound.

3.6. Analysis of the surfaces of molecular electrostatic potential (MEP)

The distribution of charge was analyzed through MEP analysis to understand how the methyl erlotinib molecule interacts with various nanostructures, including the C_{24}, $B_{12}N_{12}$, C_{32}, and $B_{16}N_{16}$ nanocages. The MEP derived from the distribution of molecular charge was characterized using the following equation:[21]

$$V(r) = \sum_A \frac{Z_A}{|R_A - r|} - \int \frac{\rho(r')dr'}{|r - r'|} \qquad (3)$$

The charge of nucleus A, denoted as Z_A, is positioned at R_A. The sign of $V(r)$ relies on which factor, the nucleus or elec-
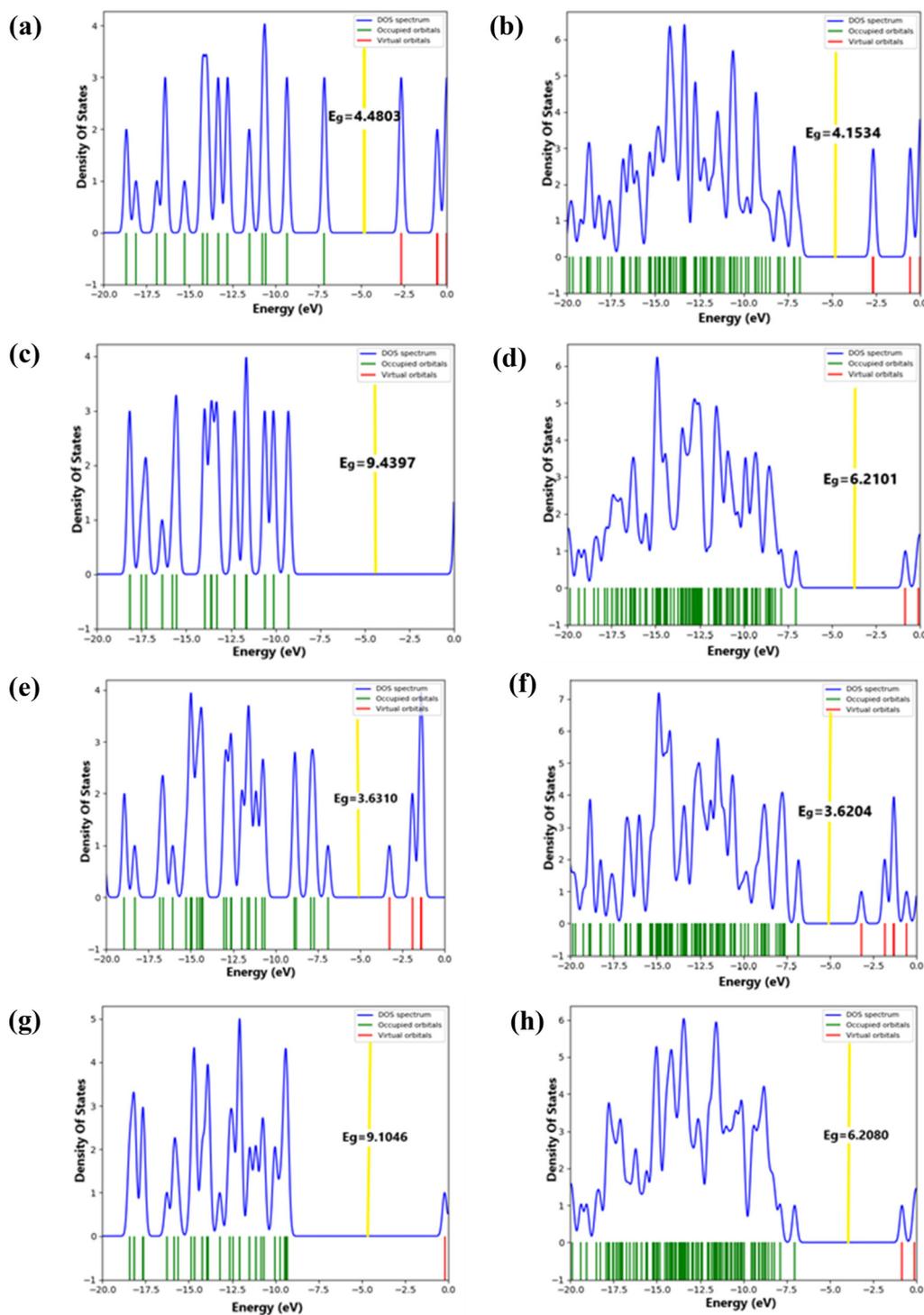
Fig. 3 (a) DOS spectra of the C_{24} nanocage, (b) methyl erlotinib@C_{24} nanocage, (c) $B_{12}N_{12}$ nanocage, (d) methyl erlotinib@$B_{12}N_{12}$ nanocage, (e) C_{32} nanocage, (f) methyl erlotinib@C_{32} nanocage, (g) $B_{16}N_{16}$ nanocage, and (h) methyl erlotinib@$B_{16}N_{16}$ nanocage. The Fermi level is represented by yellow.

trons, has a predominant effect at a particular point. According to the MEP analysis, atoms with a positive charge appeared in blue, while those with a negative charge appeared in red (see Fig. 4).[35] It is anticipated that when methyl erloti-

nib interacts with the C_{24} and C_{32} nanocages, there will be a transfer of charge from methyl erlotinib to both the C_{24} (see Fig. 4a) and C_{32} nanocages (see Fig. 4c). On the other hand, when methyl erlotinib interacts with $B_{12}N_{12}$ and $B_{16}N_{16}$,
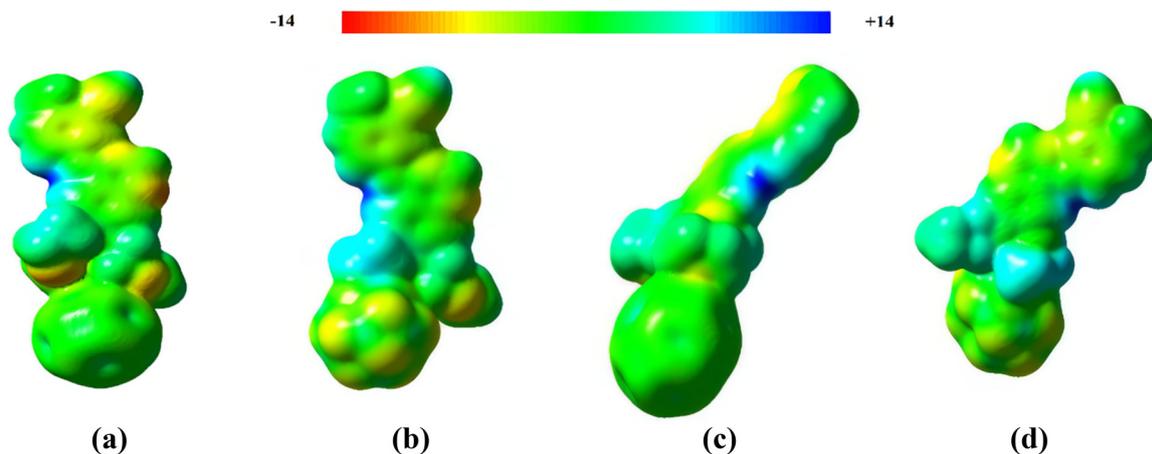
Fig. 4 Computed molecular electrostatic potential (MEP) surfaces of (a) the methyl erlotinib@C_{24} nanocage, (b) methyl erlotinib@$B_{16}N_{16}$ nanocage, (c) methyl erlotinib@C_{32} nanocage, and (d) methyl erlotinib@ $B_{16}N_{16}$ nanocage.

charge is transferred from $B_{12}N_{12}$ (Fig. 4b) and $B_{16}N_{16}$ (Fig. 4d) to methyl erlotinib. The interaction between methyl erlotinib and the nanostructures will be weak due to the transfer of charge.

3.7. FMO analysis

The energy surfaces of frontier molecular orbitals, namely the HOMO and the LUMO, indicate how effectively a molecule can accept and donate electrons. The energy difference between the surfaces of the HOMO and the LUMO serves as a valuable indicator for assessing a molecule's biological activity, kinetic stability, and chemical reactivity. Fig. 5 depicts the surfaces of the HOMO and the LUMO of methyl erlotinib when interacting with the C_{24}, $B_{12}N_{12}$, C_{32}, and $B_{16}N_{16}$ nanocages. The LUMO and HOMO orbitals are mostly focused on the methyl erlotinib medication in the methyl erlotinib@$B_{12}N_{12}$ and methyl erlotinib@$B_{16}N_{16}$ nanocages. In contrast, in the methyl erlotinib@C_{32} nanocage, the LUMO and HOMO orbitals are localized on the C_{32} nanocage itself. The HOMO orbital of the methyl erlotinib@C_{24} nanocage is positioned on the methyl erlotinib medication, while the LUMO orbital is found on the C_{24} nanocage component, implying electron transfer from methyl erlotinib to the C_{24} nanocage. Compounds possessing a small energy gap typically demonstrate lower stability and high chemical reactivity, while the opposite is true for compounds with a larger energy gap. The calculated E_g values for the methyl erlotinib@C_{24} nanocage, the methyl erlotinib@$B_{12}N_{12}$ nanocage, the methyl erlotinib@C_{32} nanocage and the methyl erlotinib@$B_{16}N_{16}$ nanocage are found to be 4.153, 6.210, 3.620 and 6.208 eV, respectively. The findings suggest that the methyl erlotinib@C_{32} nanocage system exhibits superior chemical reactivity in comparison with the other systems. The following is the order of the systems' stability:

methyl erlotinib@$B_{12}N_{12}$ nanocage > methyl erlotinib@$B_{16}N_{16}$ nanocage > methyl erlotinib@C_{24} nanocage > methyl erlotinib@C_{32} nanocage and the chemical reactivity for the systems is as follows:

methyl erlotinib@C_{32} nanocage > methyl erlotinib@C_{24} nanocage > methyl erlotinib@$B_{16}N_{16}$ nanocage > methyl erlotinib@$B_{12}N_{12}$ nanocage.

3.8. Analysis of the quantum theory of atoms in molecules (QTAIM)

Electrons are scattered within the gravitational field generated by the nuclei, as explained by the quantum theory of atoms in molecules (QTAIM). The charge density $\rho(r)$ indicates that the nucleus functions as an attractor within a cloud of negative charge. In this theory, the BCP is recognized as a collection of specific points that can be identified. Certain characteristics they possess can be utilized to identify intermolecular interactions. During crucial moments in these interactions, the distribution of electron density plays a significant role in determining the type of bond formed. The maximal charge density is exhibited by the critical point (C_P). At the BCP, the value of $\rho(r)$ reflects both the degree and strength of the bond. In this context, V_C indicates the potential electron energy density, while K_C stands for the kinetic electron energy density, and H_C signifies the electron energy density at the BCP. Given that V_C is negative and K_C is positive, Wirral's theorem indicates that the potential energy at the bond's C_p reduces significantly, leading to a negative value for $\nabla^2\rho(r)$. Based on eqn (4):

$$H_C = K_C + V_C \tag{4}$$

The $\left|\dfrac{K_C}{V_C}\right|$ ratio can be employed to assess the nature of intermolecular bonding. A value greater than 1 signifies the presence of non-covalent bonds, whereas a value ranging from 0.5 to 1 indicates the existence of partial covalent hydrogen bonds. The outcomes presented in Table 2 indicate that all examined nanocages including methyl erlotinib@C_{24}, methyl erlotinib@$B_{12}N_{12}$, methyl erlotinib@C_{32}, and methyl erlotinib@$B_{16}N_{16}$ exhibit a ratio higher than 1, implying their noncovalent nature. In this study, it is assumed that all interactions are weak because H_C is greater than zero. The inter-
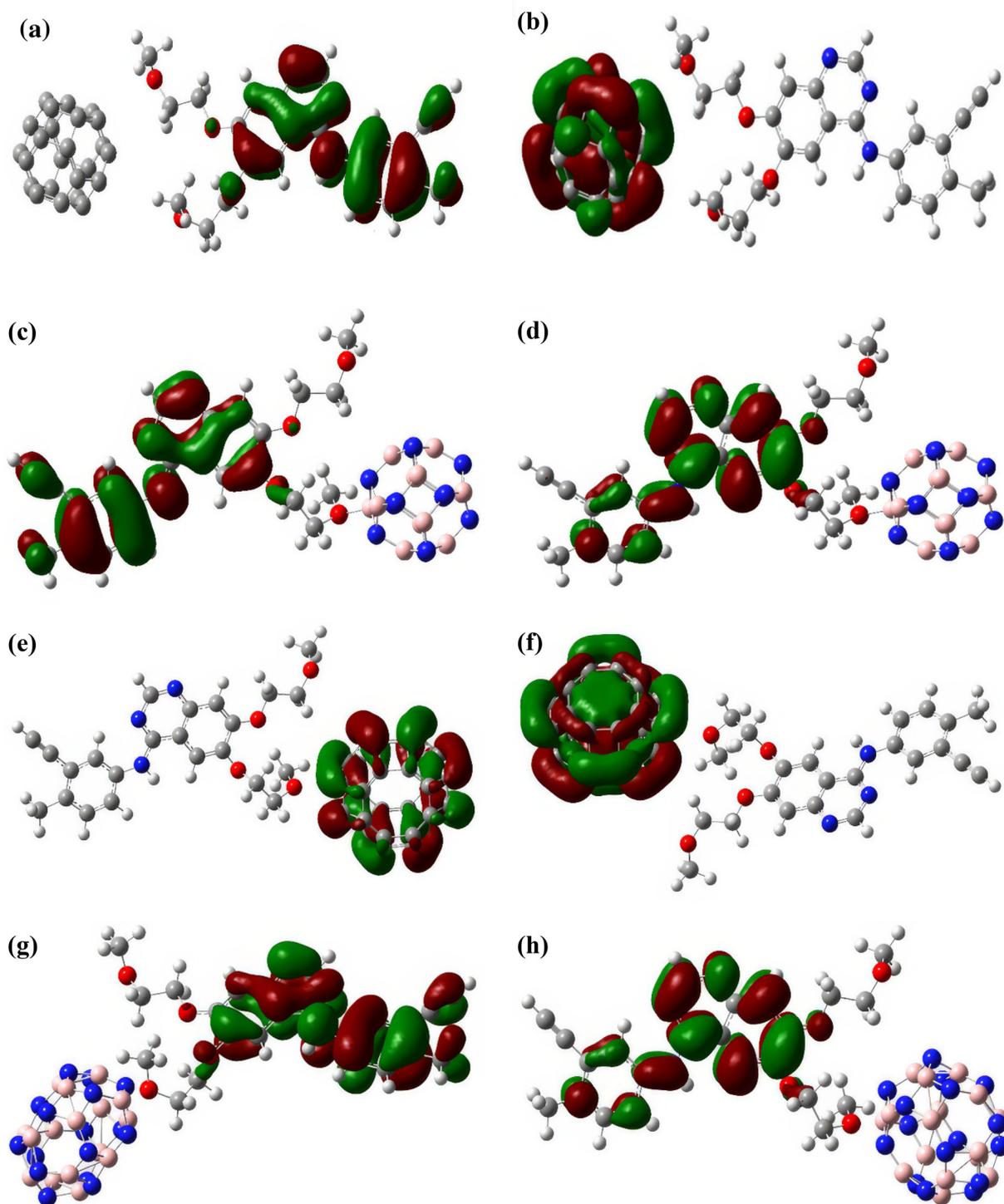
Fig. 5 FMO for the interaction of methyl erlotinib with the C_{24}, $B_{12}N_{12}$, C_{32}, and $B_{16}N_{16}$ nanocages. (a) HOMO-methyl erlotinib@C_{24} nanocage, (b) LUMO-methyl erlotinib@C_{24} nanocage, (c) HOMO-methyl erlotinib@$B_{12}N_{12}$ nanocage, (d) LUMO-methyl erlotinib@$B_{12}N_{12}$ nanocage, (e) HOMO-methyl erlotinib@C_{32} nanocage, (f) LUMO-methyl erlotinib@C_{32} nanocage, (g) HOMO-methyl erlotinib@$B_{16}N_{16}$ nanocage, and (h) LUMO-methyl erlotinib@$B_{16}N_{16}$ nanocage.

molecular interactions are described by the vital parameter of the electron density $\rho(r)$. In the examined nanostructures, the electron density ($\rho(r)$) varies considerably, spanning from 0.00239 to 0.09658 atomic units. This wide range suggests the occurrence of

diverse intermolecular forces with varying intensities. As a result, the strongest interaction is related to B_{10}–O_{35} ($\rho(r)$ = 0.09658 a.u.), whereas the weakest interaction is associated with C_{72}–H_{45} ($\rho(r)$ = 0.00239 a.u.). Molecular graphs of the optimized complexes,

Table 2 Topological characteristics at the bond critical points of interaction for the methyl erlotinib@nanostructures (a.u)

Complex	BCP	$\rho(r)$	$\nabla^2\rho(r)$	K_C	V_C	H_C	$|-K_C/V_C|$
Methyl erlotinib@C$_{24}$	C$_{22}$–H$_{69}$	0.00281	−0.00202	0.00152	−0.00050	0.00102	3.04
	C$_1$–H$_{58}$	0.00293	−0.00231	0.00181	−0.00050	0.00131	3.62
	C$_4$–H$_{55}$	0.00394	−0.00297	0.00233	−0.00064	0.00169	3.64
	C$_3$–O$_{26}$	0.00361	−0.00343	0.00271	−0.00071	0.0020	3.82
Methyl erlotinib@B$_{12}$N$_{12}$	N$_{16}$–H$_{66}$	0.01563	−0.01390	0.01240	−0.00150	0.01090	8.26
	B$_{10}$–O$_{35}$	0.09658	−0.08727	0.14352	0.05625	0.19977	2.55
	N$_{24}$–H$_{64}$	0.00727	−0.00575	0.00492	−0.00082	0.00410	6.00
	N$_{24}$–H$_{59}$	0.00499	−0.00406	0.00312	−0.00094	0.00218	3.32
	N$_{17}$–H$_{69}$	0.01432	−0.01368	0.01179	−0.00189	0.00990	6.24
Methyl erlotinib@C$_{32}$	C$_{72}$–H$_{45}$	0.00239	−0.00201	0.00156	−0.00045	0.00111	3.46
	C$_{59}$–H$_{35}$	0.00297	−0.00230	0.00174	−0.00057	0.00117	3.05
	C$_{59}$–O$_{11}$	0.00441	−0.00419	0.00338	−0.00081	0.00257	4.17
	C$_{75}$–O$_{11}$	0.00635	−0.00553	0.00468	−0.00084	0.00384	5.57
	C$_{56}$–H$_{42}$	0.00299	−0.00255	0.00198	−0.00057	0.00141	3.47
Methyl erlotinib@B$_{16}$N$_{16}$	N$_{27}$–H$_{74}$	0.01576	−0.01367	0.01231	−0.00136	0.01095	9.05
	N$_{31}$–H$_{72}$	0.00698	−0.00552	0.00471	−0.00081	0.00390	5.81
	B$_5$–O$_{43}$	0.09509	−0.08612	0.14140	0.05528	0.19668	2.56
	N$_{26}$–H$_{77}$	0.01477	−0.01389	0.01208	−0.00181	0.01027	6.67
	N$_{27}$–H$_{67}$	0.00425	−0.00350	0.00265	−0.00085	0.00180	3.12

including the methyl erlotinib@C$_{24}$ nanocage, the methyl erlotinib@B$_{12}$N$_{12}$ nanocage, the methyl erlotinib@C$_{32}$ nanocage and the methyl erlotinib@B$_{16}$N$_{16}$ nanocage, are displayed in Fig. 6. The values of E_{ads} for the methyl erlotinib@C$_{24}$ nanocage, methyl erlotinib@B$_{12}$N$_{12}$ nanocage, methyl erlotinib@C$_{32}$ nanocage and methyl erlotinib@B$_{16}$N$_{16}$ nanocage complexes indicate a weak interaction between the nanocages and the inhibitors. The

AIM outcomes for the methyl erlotinib@C$_{24}$ nanocage, methyl erlotinib@B$_{12}$N$_{12}$ nanocage, methyl erlotinib@C$_{32}$ nanocage, and methyl erlotinib@B$_{16}$N$_{16}$ nanocage complexes (see Table 2) align with the interaction trends predicted using the E_{ads} and MEP. This confirms that the C$_{24}$, B$_{12}$N$_{12}$, C$_{32}$, and B$_{16}$N$_{16}$ nanocages are effective candidates for drug delivery of the methyl erlotinib molecule.
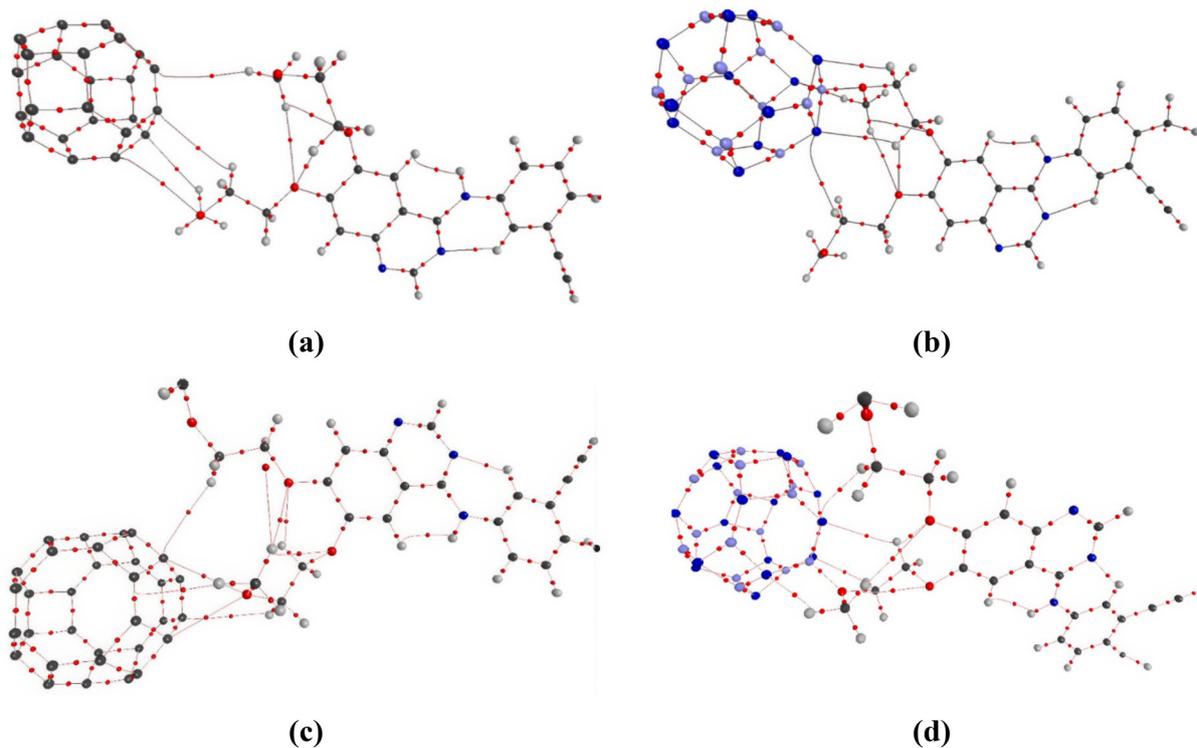

(a)

(b)

(c)

(d)

Fig. 6 Molecular graph of (a) the methyl erlotinib@C$_{24}$ nanocage complex, (b) methyl erlotinib@B$_{12}$N$_{12}$ nanocage complex, (c) methyl erlotinib@C$_{32}$ nanocage complex, and (d) methyl erlotinib@B$_{16}$N$_{16}$ nanocage complex. Small red circles represent bond critical points. The lines indicate bond paths.

3.9. Comparison of calculations from the 6-31G(d) basis set with the larger 6-311G(d,p) basis set
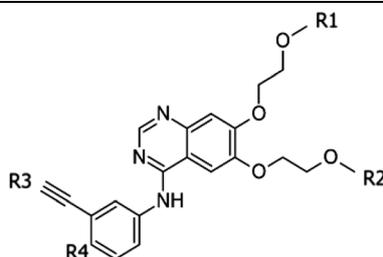
Table 3 displays computations utilizing the 6-311G(d,p) basis set, indicating that the process of methyl erlotinib adsorption across all nanocages is exothermic. Furthermore, the aqueous phase had higher adsorption energy (E_{ads}) values than that of the gas phase (with the exception of the C_{32} nanocage). The E_{ads} order is from the greatest to the least, related to the $B_{12}N_{12}$, $B_{16}N_{16}$, C_{32} and C_{24} nanocages, respectively, which aligns closely with the results obtained using the 6-31G(d) basis set. The calculations using the 6-311G(d,p) basis set revealed that both the LUMO and HOMO energy levels were lower compared to those obtained with the 6-31G(d) basis set

Table 3 Adsorption energy of methyl erlotinib onto the C_{24}, $B_{12}N_{12}$, C_{32}, and $B_{16}N_{16}$ nanocages in gaseous and aqueous phases, including the HOMO−LUMO energy gaps (E_g), BSSE, and the changes in the HOMO−LUMO gap energy during the adsorption process at the M06-2X/6-311G(d,p) level

Nanostructures	HOMO (eV)	LUMO (eV)	E_{ads} (eV) in gas	E_{ads} (eV) in water	BSSE (eV)	E_g (eV)	ΔE_g (eV)
C_{24} nanocage	−7.471	−3.040	—	—	—	4.431	—
$B_{12}N_{12}$ nanocage	−9.401	−0.051	—	—	—	9.349	—
C_{32} nanocage	−7.224	−3.641	—	—	—	3.582	—
$B_{16}N_{16}$ nanocage	−9.436	−0.397	—	—	—	9.042	—
Methyl erlotinib@C_{24} nanocage	−7.031	−3.043	−0.084	−0.110	0.001	3.988	−0.443
Methyl erlotinib@$B_{12}N_{12}$ nanocage	−7.230	−1.049	−1.107	−1.179	0.008	6.181	−3.167
Methyl erlotinib@C_{32} nanocage	−7.043	−3.551	−0.159	−0.141	0.001	3.492	−0.090
Methyl erlotinib@$B_{16}N_{16}$ nanocage	−7.236	−1.058	−1.078	−1.135	0.006	6.178	−2.863

Table 4 Models of erlotinib and its derivatives

No.	Chemspider ID	Name	R1	R2	R3	R4
E	154044	Erlotinib	CH_3	CH_3	CH	H
E1	8493030	Desmethyl erlotinib	CH_3	OH	CH	H
E2	13174069	2-[4-(3-Ethynylanilino)-7-(2-hydroxyethoxy)quinazolin-6-yl]oxyethanol	OH	OH	CH	H
E3	17349184	N-(3-Ethylphenyl)-6,7-bis(2-methoxyethoxy)-4-quinazolinamine	OH	OH	CH	H
E4	30646730	4-Methyl erlotinib	CH_3	CH_3	CH	CH_3
E5	5142935	N-(3-Ethylphenyl)-6,7-bis(2-methoxyethoxy)-4-quinazolinamine	CH_3	CH_3	C_2H_5	H

Table 5 Molecular docking results of erlotinib and some of its derivatives with TKI

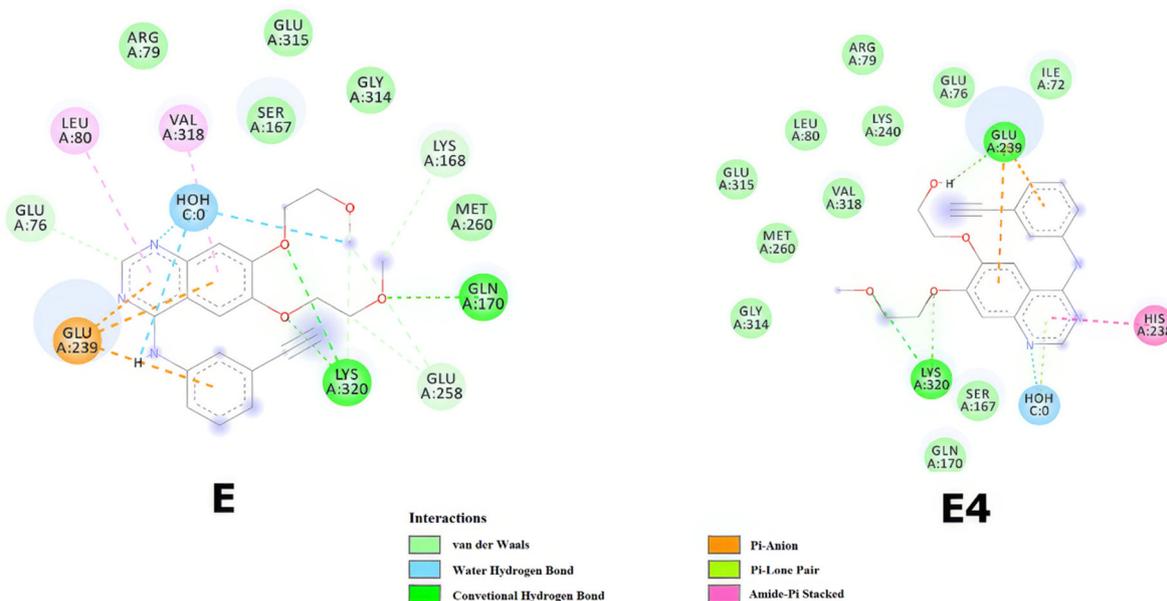| No.	E_b (kcal mol^{-1})	Interacting amino acids	
		Hydrogen bonds	Non-hydrogen bonds
E	−4.98	LYS. A:320 & GLN. A:170	ARG.A:79 & GLY.A:314 & GLU.A:315 & GLU. A:76 & GLU.A:239 & GLU.A:258 & SER. A:167 & VAL. A:318 & LEU. A:80 & HOH.C:O & LYS.A:168 & MET.A:260
E1	−4.60	LYS. A:320 & GLU. A:239	ARG.A:79 & GLY.A:314 & GLU.A:315 & GLU. A:76 & GLU.A:258 & SER. A:167 & VAL. A:318 & LEU. A:80 & HOH.C:O & LYS.A:240 & MET.A:260 & GLN.A:170 & HIS.A:238
E2	−4.89	LYS. A:320 & GLU. A:239	ARG.A:79 & GLY.A:314 & GLU. A:76 & GLU.A:258 & SER. A:167 & VAL. A:318 & LEU. A:80 & HOH.C:O & MET.A:260 & THR.A:166 & ILE.A:72 & GLN.A:170
E3	−3.83	—	GLY.A:314 & GLU. A:76 & GLU.A:239 & GLU.A:315 & SER. A:167 & VAL. A:318 & LEU. A:80 & HOH.C:O & MET.A:260 & THR.A:166 & ILE.A:72 & LYS.A:320 & HIS.A:238
E4	−5.00	LYS.A:320	PRO.A:169 & GLY.A:314 & GLU. A:76 & GLU.A:239 & GLU.A:315 & GLU.A:258 & SER. A:167 & VAL. A:318 & LEU. A:80 & HOH.C:O & MET.A:260 & LYS.A:168 & HIS.A:238 & GLN.A:170
E5	−4.48	LYS.A:320	PRO.A:169 & GLU. A:76 & GLU.A:239 & GLU.A:258 & SER. A:167 & VAL. A:318 & LEU. A:80 & HOH.C:O & MET.A:260 & ARG.A:79 & HIS.A:238 & GLN.A:170 & THR.A:166 & ILE.A:72

Fig. 7 Interacting complexes of the original E and E4 with the TKI enzyme.

and the values of energy gap (E_g) were also found to be smaller than those from the 6-31G(d) basis set.

3.10. Molecular docking (MD) simulations

Table 4 provides a list of models from this research that feature erlotinib derivatives as ligands. Molecular dynamics simulations were used to examine the interactions between each ligand structure and each TKI enzyme target separately. Values of binding energy (E_b) indicating efficacious interactions between the ligands and their targets are presented in Table 5. Furthermore, Fig. 7 provides a comprehensive overview of the names of amino acids, as well as the various kinds of non-hydrogen and hydrogen bonds present in the complex systems. Eventually, an examination of the stability of the obtained complexes reveals that E4 (4-methyl erlotinib), with a binding energy (E_b) of −5.0 kcal mol^{-1}, shows potential for effective interactions with TKI enzyme targets.

4. Conclusions

This study aimed to perform DFT calculations to explore how methyl erlotinib molecules interact with various nanostructures, including C_{24}, $B_{12}N_{12}$, C_{32}, and $B_{16}N_{16}$ nanocages. The findings demonstrated that all four nanocages were capable of interacting with methyl erlotinib, as evidenced by negative adsorption energy (E_{ads}) values in both aqueous and gaseous states. These negative E_{ads} values confirm that the adsorption of methyl erlotinib onto the nanocages is an exothermic process, indicating favorable interactions. Among the nanocages, $B_{12}N_{12}$ exhibited the strongest interaction with methyl erlotinib, followed by $B_{16}N_{16}$, C_{32}, and C_{24}, as reflected by their respective adsorption energies. Notably, the adsorp-

tion of methyl erlotinib onto $B_{12}N_{12}$ and $B_{16}N_{16}$ led to significant reductions in their energy gaps (ΔE_g), with values of −3.229 eV and −2.896 eV, respectively. This reduction in energy gaps suggests an enhancement in the conductivity of these nanostructures, making them promising candidates for applications in nanosensors.

The analysis of charge transfer, supported by the MEP results, revealed distinct mechanisms for the interaction of methyl erlotinib with the nanocages. For the C_{24} and C_{32} nanocages, charge was transferred from methyl erlotinib to the nanocages, whereas for the $B_{12}N_{12}$ and $B_{16}N_{16}$ nanocages, charge was transferred from the nanocages to methyl erlotinib. This difference in charge transfer behavior highlights the unique electronic properties of each nanocage and their varying interactions with methyl erlotinib. Despite these differences, QTAIM analysis confirmed that the interactions between methyl erlotinib and all four nanocages are weak and non-covalent, with electron density ($\rho(r)$) values ranging from 0.0023 to 0.0965 a.u. These weak interactions are advantageous for drug delivery systems, as they allow for the controlled release of methyl erlotinib at target sites. Frontier molecular orbital (FMO) analysis revealed that the chemical reactivity and stability of the methyl erlotinib–nanocage systems varied depending on the type of nanocage. Among the systems studied, $B_{12}N_{12}$ exhibited the highest stability, while C_{32} showed the highest chemical reactivity. These findings further support the potential of the $B_{12}N_{12}$ and $B_{16}N_{16}$ nanocages for applications requiring stable and efficient interactions with methyl erlotinib, such as drug delivery and sensing platforms.

In conclusion, the results of this study demonstrate that all four nanocages, C_{24}, $B_{12}N_{12}$, C_{32}, and $B_{16}N_{16}$, can effectively function as drug delivery carriers for methyl erlotinib. However, the $B_{12}N_{12}$ and $B_{16}N_{16}$ nanocages stand out due to

their superior adsorption energies, significant reductions in energy gaps, and enhanced conductivity, making them particularly suitable for applications as nanosensors. The findings underscore the importance of selecting nanocages based on their specific properties, such as conductivity, interaction strength, and charge transfer behavior, for targeted drug delivery and sensing applications. This study provides valuable insights into the design and optimization of nanocage-based systems for biomedical applications, paving the way for future research in this field.

Author contributions

All authors made substantial contributions to conception and design, acquisition of data, or analysis and interpretation of data, took part in drafting the article for important intellectual content, and agreed to be accountable for all aspects of the work.

Data availability

Data will be made available in a repository on acceptance.

Conflicts of interest

The authors declare no competing financial interest.

Acknowledgements

References

1 W. M. Eldehna, M. A. El Hassab, M. F. Abo-Ashour, T. Al-Warhi, M. M. Elaasser, N. A. Safwat, H. Suliman, M. F. Ahmed, S. T. Al-Rashood and H. A. Abdel-Aziz, Development of isatin-thiazolo [3, 2-a] benzimidazole hybrids as novel CDK2 inhibitors with potent in vitro apoptotic anti-proliferative activity: Synthesis, biological and molecular dynamics investigations, *Bioorg. Chem.*, 2021, **110**, 104748.

2 F. Li, H. Mei, X. Xie, H. Zhang, J. Liu, T. Lv, H. Nie, Y. Gao and L. Jia, Aptamer-conjugated chitosan-anchored liposomal complexes for targeted delivery of erlotinib to EGFR-mutated lung cancer cells, *AAPS J.*, 2017, **19**, 814–826.

3 D. Wang, J. Zhou, W. Fang, C. Huang, Z. Chen, M. Fan, M.-R. Zhang, Z. Xiao, K. Hu and L. Luo, A multifunctional nanotheranostic agent potentiates erlotinib to EGFR wild-type non-small cell lung cancer, *Bioact. Mater.*, 2022, **13**, 312–323, DOI: 10.1016/j.bioactmat.2021.10.046.

4 P. Pandey, K. Dua and H. Dureja, Erlotinib loaded chitosan nanoparticles: Formulation, physicochemical characterization and cytotoxic potential, *Int. J. Biol. Macromol.*, 2019, **139**, 1304–1316.

5 S. Jain, K. Dongare, B. Nallamothu, C. P. Dora, V. Kushwah, S. S. Katiyar and R. Sharma, Enhanced stability and oral bioavailability of erlotinib by solid self nano emulsifying drug delivery systems, *Int. J. Pharm.*, 2022, **622**, 121852.

6 K. M. Yang, I. C. Shin, J. W. Park, K.-S. Kim, D. K. Kim, K. Park and K. Kim, Nanoparticulation improves bioavailability of Erlotinib, *Drug Dev. Ind. Pharm.*, 2017, **43**(9), 1557–1565.

7 H. Zhong and J. Phillip Bowen, Recent, advances in small molecule inhibitors of VEGFR and EGFR signaling pathways, *Curr. Top. Med. Chem.*, 2011, **11**(12), 1571–1590.

8 H. Xu, C. He, Y. Liu, J. Jiang and T. Ma, Novel therapeutic modalities and drug delivery–erlotinib liposomes modified with galactosylated lipid: In vitro and in vivo investigations, *Artif. Cells, Nanomed., Biotechnol.*, 2018, **46**(8), 1902–1907.

9 R. Rampaka, K. Ommi and N. Chella, Role of solid lipid nanoparticles as drug delivery vehicles on the pharmacokinetic variability of Erlotinib HCl, *J. Drug Delivery Sci. Technol.*, 2021, **66**, 102886, DOI: 10.1016/j.jddst.2021.102886.

10 D. H. Truong, V. K. H. Le, T. T. Pham, A. H. Dao, T. P. D. Pham and T. H. Tran, Delivery of erlotinib for enhanced cancer treatment: An update review on particulate systems, *J. Drug Delivery Sci. Technol.*, 2020, **55**, 101348, DOI: 10.1016/j.jddst.2019.101348.

11 C. P. Dora, V. Kushwah, S. S. Katiyar, P. Kumar, V. Pillay, S. Suresh and S. Jain, Improved oral bioavailability and therapeutic efficacy of erlotinib through molecular complexation with phospholipid, *Int. J. Pharm.*, 2017, **534**(1), 1–13, DOI: 10.1016/j.ijpharm.2017.09.071.

12 S. Taghavi, M. Taghavi, M. Ghaemy, M. Farsadrooh and H. Javadian, Green and selective synthesis of sulfonated poly(pyrimidine-amides) in ionic liquid and their nanocomposites based on carboxylated MWCNTs: Investigation on photophysical, solubility, thermal, and removal of ions behaviors, *Colloids Surf., A*, 2021, **631**, 127759, DOI: 10.1016/j.colsurfa.2021.127759.

13 S. H. Khoshravesh, Z. Azizi, H. Javadian, M. Farsadrooh, N. Hashemifard, M. Soltani and M. Taghavi, Synthesis of resorcinol-functionalized multi-walled carbon nanotubes as a nanoadsorbent for the solid-phase extraction and determination of diclofenac in human plasma and aqueous samples, *Colloid Interface Sci. Commun.*, 2022, **46**, 100555, DOI: 10.1016/j.colcom.2021.100555.

14 Q. Tan, Y. Chu, M. Bie, Z. Wang and X. Xu, Preparation and Investigation of Amphiphilic Block Copolymers/Fullerene Nanocomposites as Nanocarriers for Hydrophobic Drug, *Materials*, 2017, **10**(2), 192.

15 N. Jafari and S. Zeinali, Highly Rapid and Sensitive Formaldehyde Detection at Room Temperature Using a ZIF-8/MWCNT Nanocomposite, *ACS Omega*, 2020, **5**(9), 4395–4402, DOI: **10.1021/acsomega.9b03124**.

16 C. Parlak, Ö. Alver and Ö. Bağlayan, Quantum mechanical simulation of Molnupiravir drug interaction with Si-doped C60 fullerene, *Comput. Theor. Chem.*, 2021, **1202**, 113336, DOI: **10.1016/j.comptc.2021.113336**.

17 E. B. Kalika, K. P. Katin, A. I. Kochaev, S. Kaya, M. Elik and M. M. Maslov, Fluorinated carbon and boron nitride fullerenes for drug Delivery: Computational study of structure and adsorption, *J. Mol. Liq.*, 2022, **353**, 118773, DOI: **10.1016/j.molliq.2022.118773**.

18 S. V. Prylutska, L. M. Skivka, G. V. Didenko, Y. I. Prylutskyy, M. P. Evstigneev, G. P. Potebnya, R. R. Panchuk, R. S. Stoika, U. Ritter and P. Scharff, Complex of C_{60} fullerene with doxorubicin as a promising agent in antitumor therapy, *Nanoscale Res. Lett.*, 2015, **10**, 1–7.

19 C. Misra, N. Thotakura, R. Kumar, B. Singh, G. Sharma, O. P. Katare and K. Raza, Improved cellular uptake, enhanced efficacy and promising pharmacokinetic profile of docetaxel employing glycine-tethered C60-fullerenes, *Mater. Sci. Eng., C*, 2017, **76**, 501–508, DOI: **10.1016/j.msec.2017.03.073**.

20 H. Xu, X. Tu, G. Fan, Q. Wang, X. Wang and X. Chu, Adsorption properties study of boron nitride fullerene for the application as smart drug delivery agent of anti-cancer drug hydroxyurea by density functional theory, *J. Mol. Liq.*, 2020, **318**, 114315, DOI: **10.1016/j.molliq.2020.114315**.

21 K. Mehdizadeh, F. Toiserkani, M. J. Khodabakhshi, N. Hajali and M. Farsadrooh, Investigation of drug delivery capability of single-walled carbon and boron-nitride nanotubes, boron-nitride ($B_{16}N_{16}$), and C_{32} fullerenes as nanocarriers of captopril drug; DFT study, *Diamond Relat. Mater.*, 2024, **146**, 111195, DOI: **10.1016/j.diamond.2024.111195**.

22 M. T. Baei, M. R. Taghartapeh, E. T. Lemeski and A. Soltani, A computational study of adenine, uracil, and cytosine adsorption upon AlN and BN nano-cages, *Phys. B*, 2014, **444**, 6–13.

23 J. Gong, J. W. Lam and B. Z. Tang, Benchmark and parameter tuning of hybrid functionals for fast calculation of excitation energies of AIEgens, *Phys. Chem. Chem. Phys.*, 2020, **22**(32), 18035–18039.

24 D. Jacquemin, E. A. Perpete, I. Ciofini, C. Adamo, R. Valero, Y. Zhao and D. G. Truhlar, On the performances of the M06 family of density functionals for electronic excitation energies, *J. Chem. Theory Comput.*, 2010, **6**(7), 2071–2085.

25 M. Walker, A. J. Harvey, A. Sen and C. E. Dessent, Performance of M06, M06-2X, and M06-HF density functionals for conformationally flexible anionic clusters: M06 functionals perform better than B3LYP for a model system with dispersion and ionic hydrogen-bonding interactions, *J. Phys. Chem. A*, 2013, **117**(47), 12590–12600.

26 M. Nouraliei, H. Javadian, K. Mehdizadeh, N. Sheibanian, A. S. Douk, F. Mohammadzadeh and N. Osouleddini, Fullerene carbon nanostructures for the delivery of phenelzine derivatives as new drugs to inhibit monoamine oxidase enzyme: Molecular docking interactions and density functional theory calculations, *Colloids Surf., A*, 2023, **657**, 130599, DOI: **10.1016/j.colsurfa.2022.130599**.

27 Y. Wang, P. Verma, X. Jin, D. G. Truhlar and X. He, Revised M06 density functional for main-group and transition-metal chemistry, *Proc. Natl. Acad. Sci. U. S. A.*, 2018, **115**(41), 10257–10262.

28 B. C. Yeo, D. Kim, C. Kim and S. S. Han, Pattern learning electronic density of states, *Sci. Rep.*, 2019, **9**(1), 5879.

29 N. M. O'boyle, A. L. Tenderholt and K. M. Langner, Cclib: a library for package–independent computational chemistry algorithms, *J. Comput. Chem.*, 2008, **29**(5), 839–845.

30 S. Soleimani Gorgani, M. Nouraliei and S. Soleimani Gorgani, Heterogeneous $C_{16}Zn_8O_8$ nanocluster as a selective CO/NO nanosensor: computational investigation, *Int. J. Environ. Sci. Technol.*, 2016, **13**, 1573–1580.

31 K. F. Biegler, J. Schnbohm and D. Bayles, *A program to analyze and visualize atoms in molecules*, 2001.

32 J. Pilme, E. Renault, F. Bassal, M. Amaouch, G. Montavon and N. Galland, QTAIM analysis in the context of quasirelativistic quantum calculations, *J. Chem. Theory Comput.*, 2014, **10**(11), 4830–4841.

33 G. M. Morris, R. Huey, W. Lindstrom, M. F. Sanner, R. K. Belew, D. S. Goodsell and A. J. Olson, AutoDock4 and AutoDockTools4: Automated docking with selective receptor flexibility, *J. Comput. Chem.*, 2009, **30**(16), 2785–2791.

34 S. Kim, P. A. Thiessen, E. E. Bolton, J. Chen, G. Fu, A. Gindulyte, L. Han, J. He, S. He and B. A. Shoemaker, PubChem substance and compound databases, *Nucleic Acids Res.*, 2016, **44**(D1), D1202–D1213.

35 S. Zinatloo-Ajabshir, S. Rakhshani, Z. Mehrabadi, M. Farsadrooh, M. Feizi-Dehnayebi, S. Rakhshani, M. Dušek, V. Eigner, S. Rtimi and T. M. Aminabhavi, Novel rod-like $[Cu(phen)_2(OAc)]\cdot PF_6$ complex for high-performance visible-light-driven photocatalytic degradation of hazardous organic dyes: DFT approach, Hirshfeld and fingerprint plot analysis, *J. Environ. Manage.*, 2024, **350**, 119545, DOI: **10.1016/j.jenvman.2023.119545**.